catalysts

MDPI

Article

Visible Light Photocatalytic Degradation Performance of Metal (Fe, Ce, Ni, Mn, Bi)-Doped Sodium Tantalite Perovskite

Aijun Huang [1], Haijuan Zhan [1,*], Meng Wen [1], Yao Zhou [1], Shuxian Bi [1], Wanyi Liu [1] and Feng Li [2,*]

[1] State Key Laboratory of High-Efficiency Utilization of Coal and Green Chemical Engineering, National Demonstration Center for Experimental Chemistry Education, College of Chemistry and Chemical Engineering, Ningxia University, Yinchuan 750021, China
[2] State Key Laboratory of Coal Conversion, Institute of Coal Chemistry, Chinese Academy of Sciences, Taiyuan 030001, China
* Correspondence: drzhj1225@126.com (H.Z.); lifeng2729@sxicc.ac.cn (F.L.)

Abstract: Metal ion doping is the most widely used means to improve the photocatalytic performance of semiconductor materials, which can adjust the band gap, broaden the range of optical response and construct impurity levels. The high efficiency modified $NaTaO_3$ perovskite catalyst with good structural and catalytic properties was synthesized by a simple hydrothermal reaction method. A variety of analysis and testing techniques, such as XRD, SEM, DRS, XPS and EPR, were used to analyze the structure properties of the prepared materials. The results show that the influence mechanism of different metal introduction on the structure and properties of the $NaTaO_3$ perovskite was different. Metal doping promoted the bond angle of Ta-O-Ta close to 180°, which restrains the recombination of the photogenerated electron-holes in the crystal. As Ce is introduced into the perovskite, the CeO_2 forms and agglomerates around the perovskite, which improves the electron transport performance. With the narrower band gap, the Ce-modified perovskite shows that the degradation rate of ARS is 84% after 180 min of photoreaction. The species of h^+, O^{2-} and ·OH play different roles in improving the performance of the photocatalytic degradation process.

Keywords: perovskite; photocatalytic degradation; modification; organic dyes

Citation: Huang, A.; Zhan, H.; Wen, M.; Zhou, Y.; Bi, S.; Liu, W.; Li, F. Visible Light Photocatalytic Degradation Performance of Metal (Fe, Ce, Ni, Mn, Bi)-Doped Sodium Tantalite Perovskite. *Catalysts* **2023**, *13*, 1250. https://doi.org/10.3390/catal13091250

Academic Editor: Vincenzo Vaiano

Received: 4 July 2023
Revised: 18 August 2023
Accepted: 24 August 2023
Published: 29 August 2023

1. Introduction

Water pollution is a serious threat to human survival and health. However, with the rapid development of the social economy, more and more wastewater containing organic pollutants has been produced. The dye-organic matter has aroused great concern due to its high toxicity [1,2]. At present, the main methods of dealing with dye wastewater include the physical method [3], chemical method [4], biological method [5], electrochemical method [6] and emerging photocatalytic degradation method [7]. Among them, photocatalytic technology has attracted much attention because of its green and high efficiency [8,9]. It is worth noting that high efficiency and application in visible range are the requirements of the development of photocatalysis technology. The development of efficient and stable catalysts is key to realizing the breakthrough of photocatalysis technology.

At present, a variety of materials such as metal oxides [10], metal sulfides [11], perovskite-type oxides [12], carbon nitride polymers [13] and so on are used for the photocatalytic process, especially for the photocatalytic degradation of dye wastewater. However, these materials still have some problems, such as narrow light harvesting, a short lifetime of photoinduced charges, and low efficiency and stability [14]. It is well known that the properties of the catalytic material itself, such as the band gap width and absorptivity, are related to photocatalytic activity. Moreover, the oxygen vacancy defect and the electron cloud density around active sites also affect the performance of the catalysts [15]. Thus, it is an important way to obtain excellent photocatalysts to improve the photocatalytic performance of materials with good band-gap properties by regulating oxygen vacancy

defects and electron cloud density by different means. The perovskite is a kind of hot spot material in the photocatalytic field due to its unique structure and photoelectric properties. $NaTaO_3$ is considered a promising member in the perovskite family for photocatalytic degradation due to its good structure and high charge separation efficiency. However, the narrow light response range restricts its development and application. In order to further improve the photocatalytic activity of $NaTaO_3$, several investigations have been carried out, such as ion doping, noble metal loading and heterojunctions structure building. Among them, ion doping has been considered as a simple and effective modification method. The $NaNb_xTa_{1-x}O_3$ shows high photocatalytic activity since Nb doping improves the specific surface area and narrowed band gaps compared with $NaTaO_3$ [16]. La-doped $NaTaO_3$ shows an improvement in both the crystalline structure and quantum yield, which enhances photocatalytic activity [17]. Introducing Mg^{2+}, Ca^{2+} and Sr^{2+} can reduce the band gap for $NaTaO_3$, which is beneficial to photocatalytic degradation [18]. Significantly, the properties of doping elements and their atomic radius are very important to the structure and properties of $NaTaO_3$, given the constraints of the perovskite material structure tolerance factor [19]. Therefore, Ce, Bi, Mn, Fe and Ni were selected as dopants for $NaTaO_3$ in this study. The atomic radius sequence is Na (1.91 Å) > Ce(1.82 Å) > Bi(1.70 Å)> Ta(1.48 Å) > Mn(1.32 Å) > Fe(1.27 Å) > Ni(1.24 Å) > O(0.66 Å) for all involved elements.

Herein, we introduce these elements into the $NaTaO_3$ perovskite structure in order to investigate the influences of the dopants for the structure properties and widen the optical response range, improve the ability of photogenic electron-hole separation, and finally enhance the photocatalytic performance for the prepared catalysts. The prepared doped $NaTaO_3$ materials were denoted as Bi-NTO, Fe-NTO, Ce-NTO, Ni-NTO and Mn-NTO, respectively. The photocatalytic activity of the doped-$NaTaO_3$ was investigated by degrading methylene blue (MB) and alizarin red S (ARS) under visible light. The detail structure and optical properties were discussed, and the mechanism of photocatalytic degradation reaction was also described.

2. Results and Discussion

2.1. Characterization of Catalyst

2.1.1. XRD Analysis of Catalysts

The XRD results (Figure 1a) show that the $NaTaO_3$ perovskite structure is the main crystalline phase for all the samples. Except for the sample with Bi doping, no impurity peak appeared in other samples. This indicates that the crystal phase of the perovskite structure can be stably maintained with metal element doping [20]. The crystal plane has different degrees of deviation to the direction of the low angle in the enlarged image (Figure 1b), resulting in an increase in crystal plane spacing d for the samples with Fe, Ce, Ni and Mn doping. The phase of metal Bi can be observed in the XRD pattern, and the strongest diffraction peak shifts to the high angle direction for the Bi-NTO sample. It indicates the low solid solubility of Bi for the $NaTaO_3$ perovskite structure, which may also be the reason for the weak diffraction peak strength of $NaTaO_3$ [21]. Commonly, substitution is more likely to occur in the perovskite structure between elements with a similar ionic radius [20]. Thus, in our catalysts system, Fe, Ni and Mn tend to take the place of Ta while Ce and Bi might partially replace Na in the $NaTaO_3$ perovskite structure (rNa^+ = 1.39 Å, rTa^{5+} = 0.64 Å, rFe^{3+} = 0.64 Å, rCe^{3+} = 1.14 Å, rNi^{3+} = 0.69 Å, rMn^{3+} = 0.58 Å, rBi^{3+} = 1.03 Å).

Table 1 shows the analysis and calculation of catalyst cell parameters and cell volume based on XRD parameters, showing that $NaTaO_3$ and M-$NaTaO_3$ (M = Fe, Ce, Ni, Mn, Bi) are monoclinic crystalline perovskites (a = 3.90627 Å, b = 3.90789 Å, c = 3.90251 Å, and M-$NaTaO_3$. PDF#74-2479), the intrinsic cell volume of $NaTaO_3$ is 58.85 [A^3], and after Fe, Ce, Ni and Mn doping, the cell volume decreases, and the cell system becomes more stable. After the introduction of metal Bi, the grain size and cell volume increase.

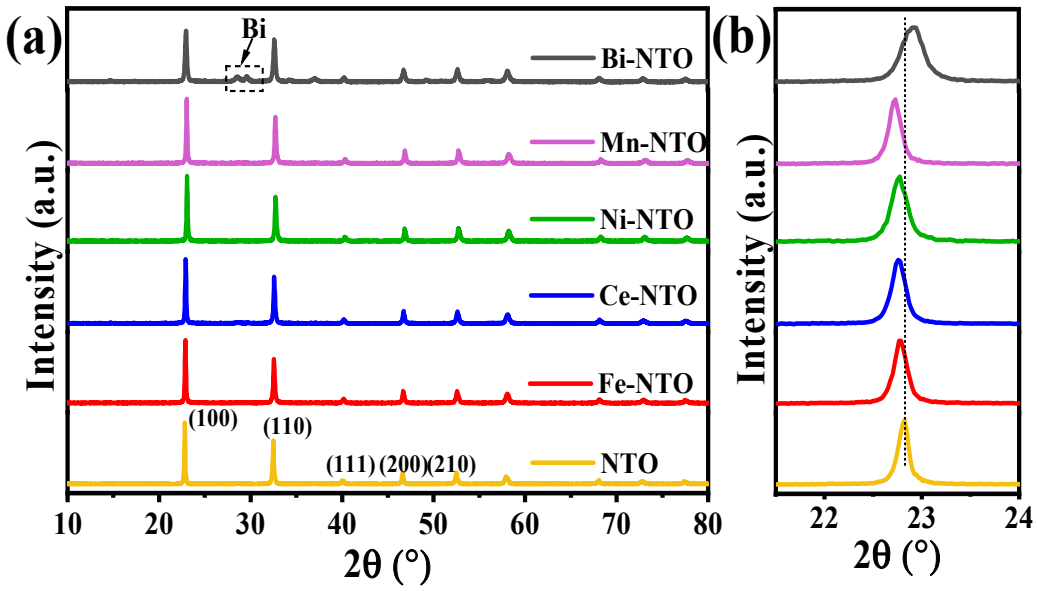

Figure 1. (**a**) The XRD patterns of the prepared samples; (**b**) the enlarged image of the strongest peak.

Table 1. Crystal parameters of $NaTaO_3$ and M-$NaTaO_3$ (M = Fe, Ce, Ni, Mn, Bi) by XRD.

Samples	NTO	Fe-NTO	Ce-NTO	Ni-NTO	Mn-NTO	Bi-NTO
a [Å]	3.8811	3.8925	3.8839	3.9048	3.8714	3.8782
b [Å]	3.8870	3.8936	3.8881	3.8651	3.8765	3.8902
c [Å]	3.9095	3.8886	3.8892	3.8957	3.9135	3.9062
Vol [$Å^3$]	58.85	58.83	58.73	58.79	58.73	58.94

2.1.2. FT-IR Analysis of Catalysts

Figure 2 shows the FT-IR spectra of the catalysts, from which the functional groups of $NaTaO_3$ did not change significantly after the introduction of different metals. The absorption peaks at the 3684 cm^{-1} and 1060 cm^{-1} wave number are the hydroxyl peaks adsorbed on the surface of the sample [22]. The signal in the range of 500–700 cm^{-1} belongs to the Ta-O-Ta stretching vibration [23]. From Figure 2b, it can be seen that with the doping of different metals, the Ta-O-Ta absorption peaks are shifted to different degrees in the direction of a high wave number, indicating that different metal doping will have a certain effect on the absorption peak position. The Ta-O-Ta bond angle in $NaTaO_3$ is 163°, and with the metals doping, this value moves closer to 180°. It should be noted that the larger bond angle leads to a lower photo-generated electron-hole recombination rate inside the crystal, which indicates the introduction of metal to reduce the compounding of the electron-hole [24]. Meanwhile, the characteristic absorption peaks of the stretching vibrations of metals, such as Fe-O, Ce-O, Ni-O, Mn-O and Bi-O, were not found in the spectra. It is probably due to the coincidence of the metal–oxygen bond with the Ta-O bond at the range of 500–700 cm^{-1}.

2.1.3. XPS Analysis of Catalysts

Figure 3a shows the full spectrum of the prepared catalysts, which shows that the catalyst contains Na, Ta, O and the doped metals Fe, Ce, Ni, Mn and Bi. Further fitting the XPS spectrum, Na 1s is located at 1070~1080 eV binding energy, Ta 4f is located at 22~32 eV binding energy and O 1s is located at 526~538 eV binding energy (the detailed information of O 1s profiles was presented in Figure S1). Figure 3b shows the high-resolution XPS spectra of Ta 4f, and the dual energy state of Ta 4f is consistent with the oxidation state of Ta^{5+} [25], mainly in the form of $NaTaO_3$. The peaks were mainly concentrated in Ta $4f_{7/2}$ at 25.37 eV binding energy and Ta $4f_{5/2}$ at 27.27 eV binding energy. It can be seen that the Ta 4f diffraction peak has an obvious displacement change after metal doping. The

introduction of metal Fe, Ni and Mn led to the shift to a lower binding energy direction of Ta 4f. This phenomenon indicates that Fe, Ni and Mn mainly occupy the Ta position in the $NaTaO_3$ perovskite. After the introduction of metals Ce and Bi, the binding energy of the Ta 4f diffraction peak moves to a higher direction, which indicates that the introduction of metals Ce and Bi mainly occupies the Na site.

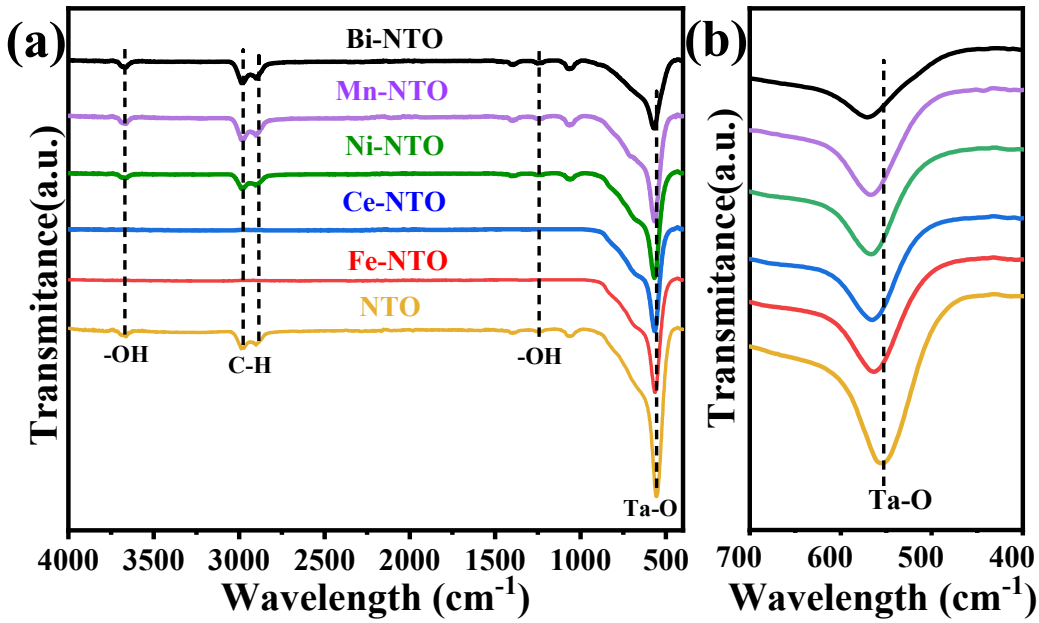

Figure 2. (**a**) FT-IR diagram of $NaTaO_3$ and M-$NaTaO_3$ (M = Fe, Ce, Ni, Mn, Bi); (**b**) the enlarged image of Ta-O vibration.

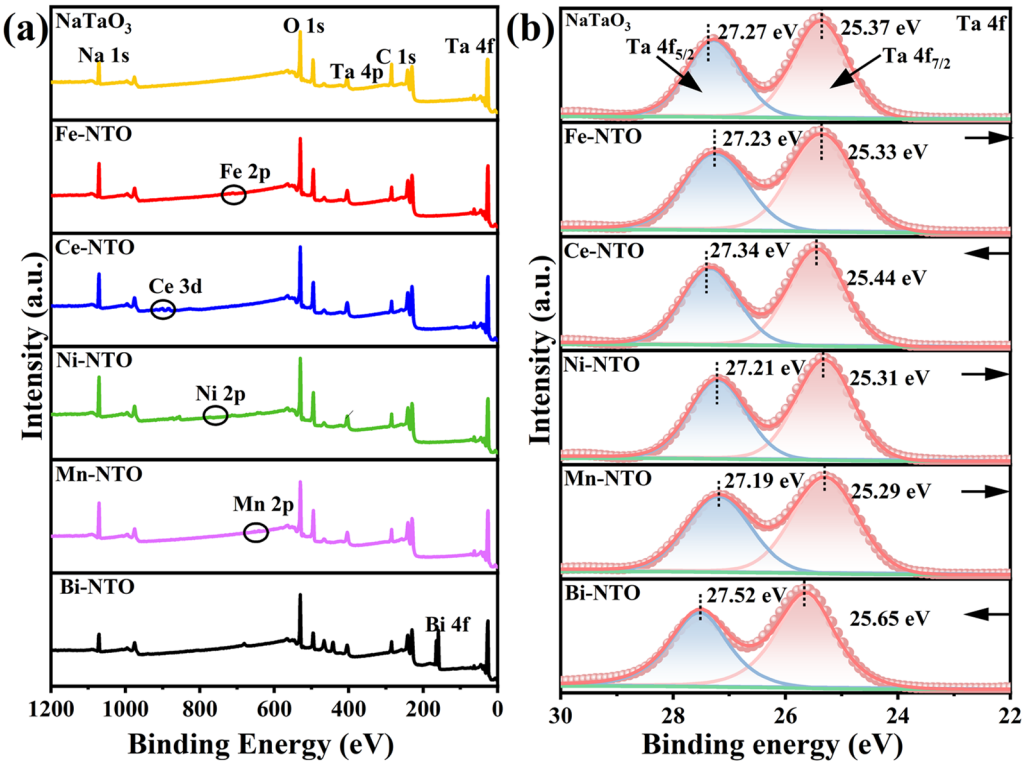

Figure 3. (**a**,**b**) Shows the full spectra of the prepared samples and Ta 4f high-resolution XPS.

The species and content of surface oxygen might have a strong influence on catalyst activity. The surface oxygen species for the samples were analyzed and the results are

shown in Figure 3 and Table 2. The oxygen species on the prepared catalyst surface mainly include lattice oxygen (O^{2-}) near 529 eV, adsorbed oxygen (O^{-}/O_2^{-}) near 530 eV and adsorbed water near 533 eV [26]. Table 2 shows the percentage content of each oxygen species on the catalyst surface. The content of lattice oxygen increased for the doped sample except for Mn-NTO, and the Ce-doped sample increased the most, compared with NTO. Fe^{2+}/Fe^{3+}, Ce^{3+}/Ce^{4+}, Ni^{2+}/Ni^{3+}, Mn^{2+}/Mn^{4+}, Bi^{3+} and metallic Bi were found in Figure S2, which is consistent with the literature [27,28]. The lowest O^{2-} and highest O^{-}/O_2^{-} for Mn-NTO aligned with the closest radius for Mn and Ta [28].

Table 2. Percent oxygen content of O1s elements in $NaTaO_3$ and M-$NaTaO_3$ (M = Fe, Ce, Ni, Mn, Bi).

Samples	NTO	Fe-NTO	Ce-NTO	Ni-NTO	Mn-NTO	Bi-NTO
O^{2-} (%)	67.07	76.93	82.75	77.44	57.68	79.70
O^{-}/O_2^{-} (%)	26.79	10.09	8.19	13.83	30.39	17.28
Absorbed water (%)	6.14	12.98	9.06	8.73	11.93	3.02

2.1.4. SEM Analysis of Catalysts

The morphology of the catalyst was investigated by SEM, and Figure 4a,c show SEM images of the neat $NaTaO_3$ at different scales. It can be seen from the figures that the neat $NaTaO_3$ has a typical nanocubic structure with highly smooth, regular and ordered surfaces stacked on top of each other. Figure 4d,e show SEM images of Ce-NTO at different scales, and it can be seen that the nanocubic structure was kept for Ce-NTO. The particle size distribution of neat $NaTaO_3$ is located at the range of 200–400 nm, with an average particle size of 273.61 nm after measurement. The average particle size of Ce-NTO is 248.6 nm within the same range. This means that metal doping leads to particle size reduction. Particle size is an important factor affecting the photocatalytic activity for the materials, and the smaller the particle size, the shorter the migration distance during the migration of photogenerated electrons and holes on the photocatalyst surface, which may be more favorable to the photocatalytic performance [29]. Therefore, as the particle size decreases after metal doping, the electrons and holes might react with the dye molecules more efficiently, which may lead to higher photocatalytic degradation activity. The EDS pattern of the Ce-NTO sample has shown the existence of Na, Ta, O and Ce, indicating the successful doping of Ce.

2.1.5. TEM Analysis of Catalysts

The surface of neat $NaTaO_3$ is regular and orderly in the TEM image (Figure 5a), and both the (100) and (110) crystal planes are the main exposed crystal faces (Figure 5d). The rod and particle agglomeration morphologies can be observed around the perovskite for the Ce-NTO sample. The phenomenon might contribute to the compactness electronic transmission. Moreover, the (111) crystalline plane of CeO_2 also exists in the Ce-NTO sample, and the lattice spacing of NTO becomes larger because of the larger ionic radius of Ce, which is consistent with the XRD results (Figure 5f). The larger lattice spacing of the (100) crystal plane for the $NaTaO_3$ of Fe-NTO and Ni-NTO can be found due to the substitution of Ni^{3+} and Fe^{3+} for Ta^{5+} with the large ionic radii in the perovskite structure. The (004) crystal plane of MnO_2 with interlocking lattice stripes can be observed together with the (110) crystal plane of NTO for the Mn-NTO sample, demonstrating the presence of some of the Mn in the form of oxides. The lattice spacing for the (100) crystalline plane of $NaTaO_3$ diminishes with Bi doping, which is consistent with the XRD results.

Combined with the TEM and XRD results, it is speculated that the crystalline structure of the catalysts has been changed with the metal elements doping. The Fe^{3+}, Ni^{3+} and Mn^{4+} elements with larger ionic radii have replaced some of the Ta elements in $NaTaO_3$, and Ce^{3+} and Bi^{3+} have replaced some of the Na elements in $NaTaO_3$ during the preparation process. As a result, the catalyst contains a variety of different M-O metal–oxygen bonds. During the process of crystal integration, the metal–oxygen bonds rearrange and combine to form

the perovskite structure due to the different bond lengths, resulting in the distortion of the crystal surface structure and the formation of crystal defects.

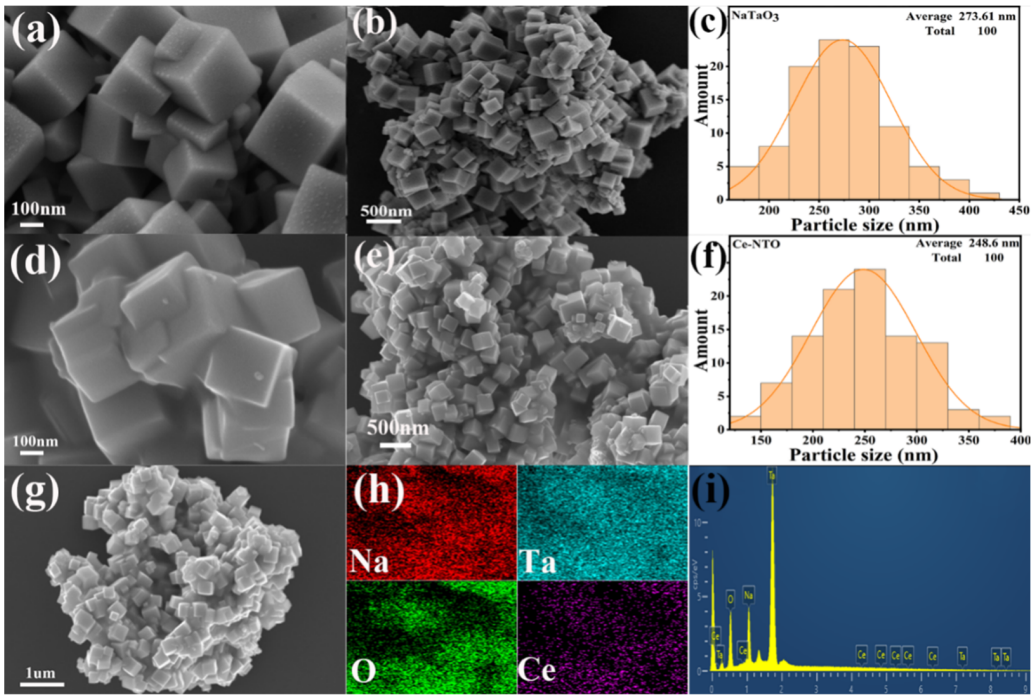

Figure 4. (**a**–**c**) SEM diagram, particle size distribution of NTO; (**d**–**f**) SEM image and particle size distribution of Ce-NTO; (**g**–**i**) SEM, Mapping, EDS mapping of Ce-NTO.

2.1.6. Catalyst UV-Vis-DRS Analysis

The UV-Vis diffuse reflectance spectra (DRS) provide a visual representation of the range and extent of the light response of the materials. As can be seen from Figure 6a, the pure phase of $NaTaO_3$ only has a light absorption response in the UV region, with the absorption edge at 308 nm. The absorption edges of the five groups of elements doped showed different degrees of redshift. The light response of Fe- and Mn-doped $NaTaO_3$ is expanded from the original pure ultraviolet light response to the visible light region. The analysis results suggested that the introduction of metal can effectively reduce the band gap value of $NaTaO_3$ (Figure 6b), and the narrow band gap is beneficial to improving the light absorption ability of the material and producing more photogenerated electron-hole pairs under visible light irradiation, which increases the photocatalytic activity of the material.

Figure 6c,d show the VB-XPS spectra of $NaTaO_3$ and Ce-$NaTaO_3$, and according to the equation $E_{CB} = E_{VB} - E_{g(2\text{-}1)}$, the CB of the catalysts were −1.23 eV, −0.49 eV, −1.42 eV, −1.88 eV, −0.44 eV, −0.67 eV. and −1.42 eV for the catalysts, compared to the intrinsic $NaTaO_3$ (4.02 eV). The VB XPS spectrum of all catalysts was presented in Figure S3. Moreover, the band gap of the catalyst Ce-$NaTaO_3$ is narrowed, and the narrow band gap improves the light absorption. It can be summarized that the valence band increased with Ce doping, which might increase the migration rate of photogenerated carriers, reduce the compounding efficiency of photogenerated charges and holes, and enhance the photoactivity.

2.1.7. Photoluminescence (PL)

Figure 7 shows the PL spectra of all prepared materials at a 370 nm photoexcitation wavelength. All materials exhibit different degrees of photoluminescence properties at 420–550 nm. It can be seen that the emission intensity of the metal-doped perovskites decreases significantly compared with the neat $NaTaO_3$ except for Bi-NTO, which indicates the lower photogenerated electron-hole recombination rate of the doped materials. The

sharp decrease in the emission intensity for the Fe, Ni and Mn doped samples indicates that the substitution of Ta^{5+} distorts the lattice structure and reduces the band gap of the material. This leads to higher photogenerated carrier mobility and a reduced complexation of photogenerated electrons and holes. Moreover, lower energy is required for the photocatalytic process, which is in agreement with the results for solid UV.

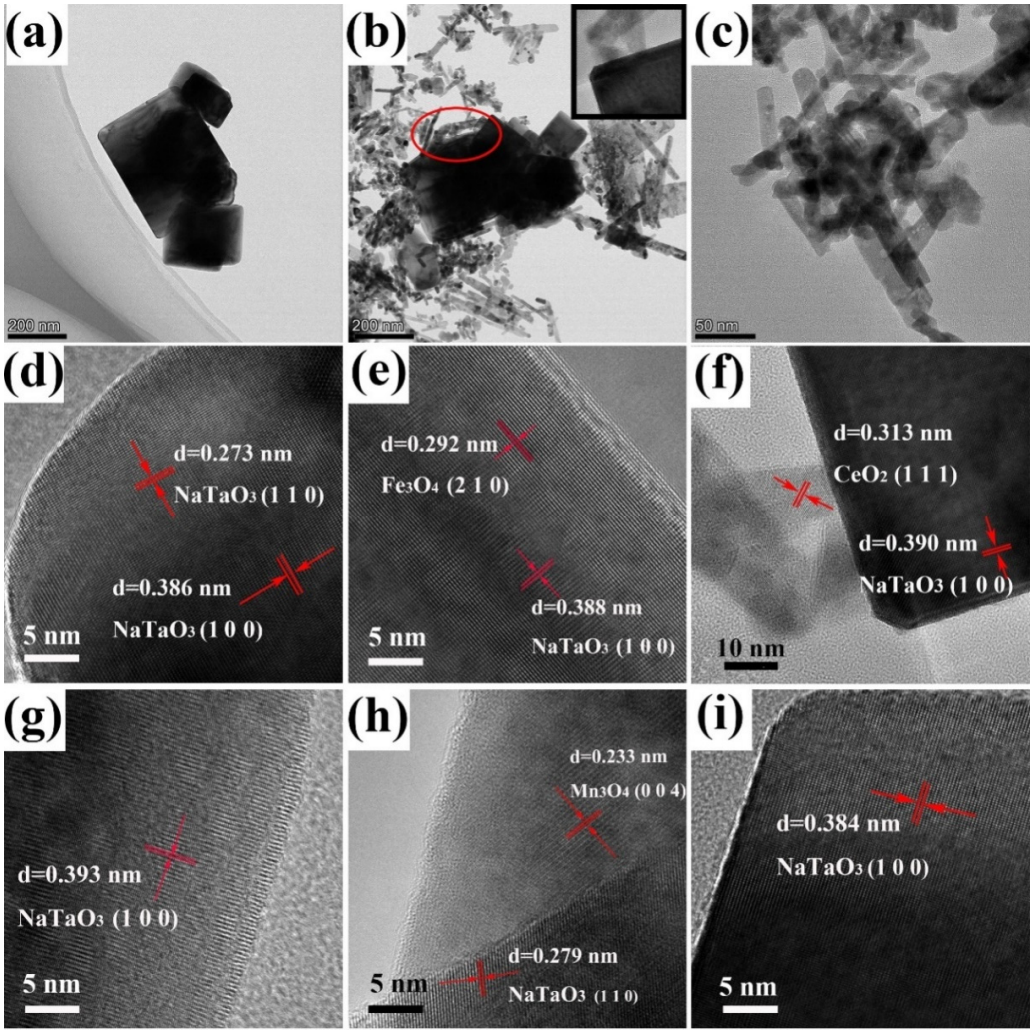

Figure 5. (**a**) TEM images of NTO; (**b**,**c**) TEM images of Ce-NTO; (**d**–**i**) HRTEM images of NTO, Fe-NTO, Ce-NTO, Ni-NTO, Mn-NTO, Bi-NTO.

2.2. Photocatalytic Degradation Performance

In order to investigate the activity of the prepared catalysts in photocatalytic degradation, methylene blue and alizarin red were selected as substrates for photocatalytic degradation evaluation. From Figure 8a, it can be seen that the adsorption amounts of all the samples on methylene blue were basically the same in the first 30 min, indicating that the doping of metals did not change the surface charge and surface morphology of NTO. Under visible light, the photocatalytic activity of the catalysts showed the pattern of Ce-NTO > Ni-NTO > Fe-NTO > Bi-NTO > NTO > Mn-NTO, which is consistent with the change pattern of lattice oxygen from the analysis of XPS. Figure 8c depicts the photocatalytic activity of the catalyst for the degradation of ARS in visible light. It can be seen that the metal doped samples present better photocatalytic degradation performance on the whole, which indicates the effect of metal doping on photocatalytic degradation performance improvement. The Ce-doped catalyst showed the best photocatalytic degradation performance for both MB and ARS.

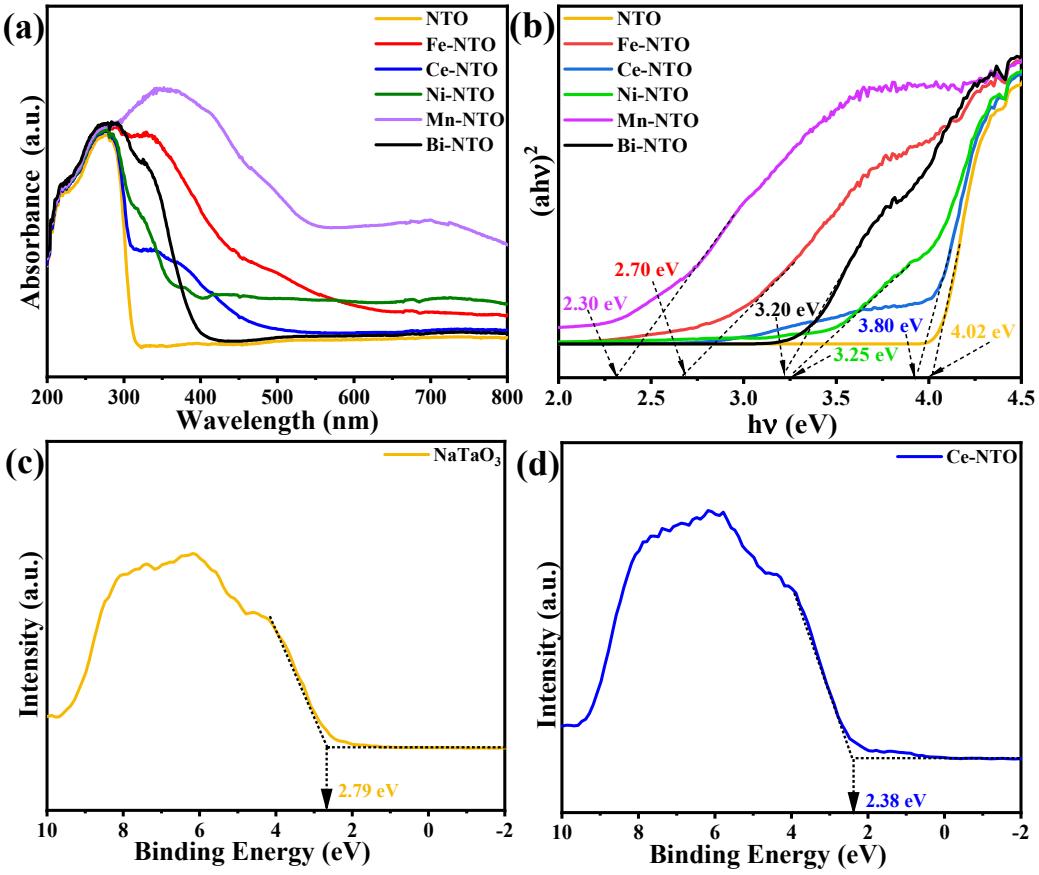

Figure 6. (**a**,**b**) UV-Vis absorption spectra and energy band diagrams of the catalysts (**c**,**d**) are the VB XPS spectra of the catalysts.

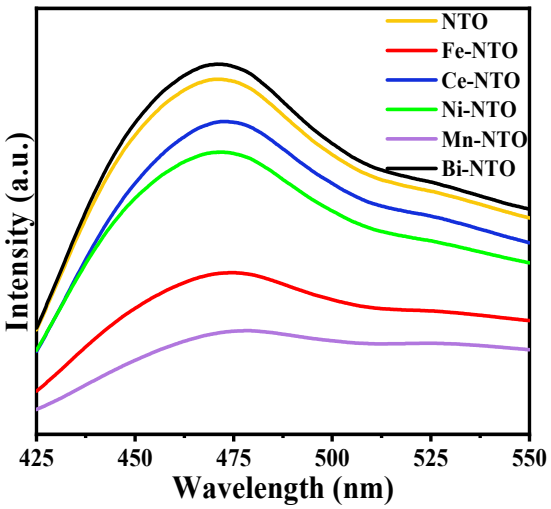

Figure 7. Photoluminescence spectra of $NaTaO_3$ and M-$NaTaO_3$ (M = Fe, Ce, Ni, Mn, Bi) series catalysts.

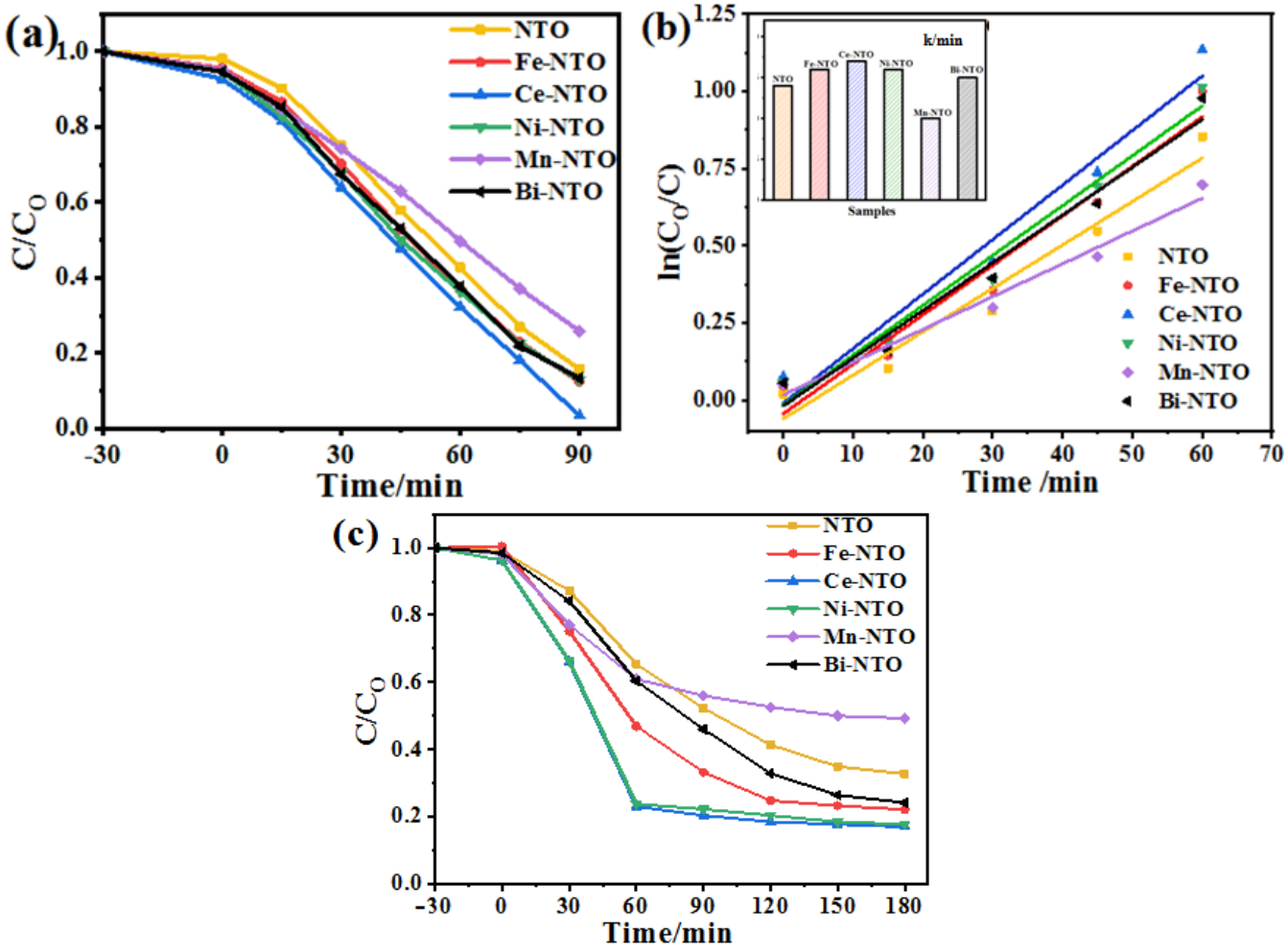

Figure 8. (**a**,**b**) Shows the photocatalytic degradation MB curves and primary kinetics; (**c**) shows the photocatalytic degradation ARS curves.

To understand the reaction kinetic behavior of each catalyst for pollutant degradation, the MB and ARS degradation data were further fitted by pseudo primary kinetics. As shown in Figure 8b, the reaction between $\ln(C/C_0)$ and light time conforms to quasi-first-order kinetics: $\ln(C/C_0) = kt$, k is the apparent reaction rate constant. The histogram shows that the photodegradation rate constant of metal-doped $NaTaO_3$ is higher than that of the pure phase $NaTaO_3$. For the photocatalytic degradation of ARS, the samples show the different kinetics. The Ce-NTO and Ni-NTO sample present the linear fit within just 60 min (as shown in Figure S4).

The results show that the introduction of metal can effectively reduce the band gap value of $NaTaO_3$, and a narrow band gap is beneficial to improving the light absorption capacity of the material. Among them, the optical response of Fe-, Ce-, Ni-, Mn- and Bi-doped $NaTaO_3$ is broadened from the original $NaTaO_3$ pure ultraviolet light response to the visible light region. The presence of CeO_2 after metal Ce doping increases the absorption strength of the material, which is consistent with the literature reports [30]. More photogenerated electron-hole pairs are generated under visible light irradiation, thus improving the photocatalytic activity of the material. The Mn-doped catalysts showed outstanding advantages in visible light expansion and photoelectron excitation energy, but the photocatalytic degradation experiments of ARS and MB (the photocatalytic degradation rate of the sample Mn-NTO was lower than that of the sample $NaTaO_3$) showed that while the narrow band gap is conducive to improving light absorption capacity, it does not necessarily lead to better or worse photocatalytic activity. It tends to a certain limit.

In order to investigate the stability of the catalyst, the cyclic photocatalytic degradation of ARS under visible light irradiation was investigated by cycling the photocatalyst Ce-NTO. The degradation rate of the catalyst decreased after four consecutive cycles of degrading ARS (Figure 9a), but still reached 78%. The decrease in the degradation rate may be due to the adsorption of some pollutant molecules on the catalyst surface, causing pore blockage. However, the photocatalyst still had a high stability. In addition, the XRD patterns of the fresh and used Ce-NTO samples after recycling were displayed in Figure 9b. The results mean that the perovskite structure keeps stable after cycle use, although the diffraction peak intensity decreased slightly.

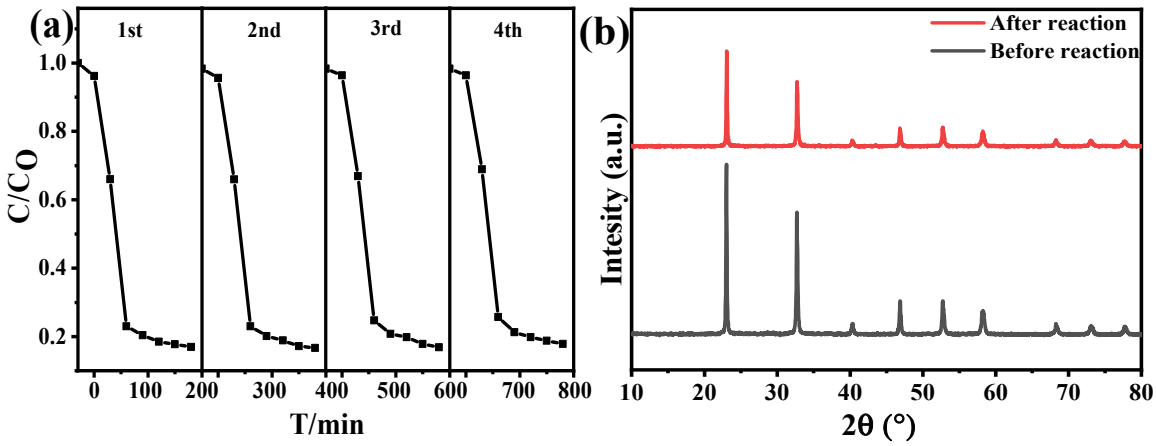

Figure 9. (**a**) Ce-NTO degradation of AR cycle experiment; (**b**) XRD comparison of catalyst Ce-NTO before and after use.

2.3. Photocatalytic Degradation Mechanism

Figure 10a shows the effects of different scavengers on the degradation rate of ARS within 180 min. It can be seen that the addition of scavengers can inhibit the degradation rate of ARS, and the inhibition sequence is EDTA-2Na > IPA > BQ. The h^+, $\cdot O_2^-$ and ·OH play a different role in the process of degradation. The h^+ is the main active substance for pollutant degradation. Figure 10b shows the signal of the spin capture reagent TEMPO. The signal intensity is weakened after light when TEMPO (2,2,6,6-Tetramethylpiperidinooxy) is combined with h^+ to form $TEMPO^+$.

The excited electrons jump from the valence band to the conduction band, leaving the active h^+ in the valence band for Ce-NTO during the photocatalytic process. As shown in Figure 10c,d, almost no O_2^- and ·OH signals fluctuate in the dark. The DMPO-$\cdot O_2^-$ (5,5-Dimethyl-1-pyrrolidine N-oxide) and DMPO-OH show obvious characteristics of four lines for the EPR signal after visible light irradiation, which displays the production of $\cdot O_2^-$ and ·OH in the process of degradation. It can be concluded from the results of a free radical experiment and EPR (electron paramagnetic resonance) test that the h^+, $\cdot O_2^-$, and ·OH species play different roles in the process of photocatalytic degradation, and that h^+ and $\cdot O_2^-$ are the main active substances.

Based on the results and analysis above, a possible mechanism for the photocatalytic degradation of pollutants is proposed to illustrate the excellent photocatalytic activity of Ce-NTO (Figure 11). According to the TEM results, it can be clearly seen that the lattice expansion and increase in cell volume and impurity defects were caused by Ce doping in the structure. These produce more oxygen vacancies and reduce carrier recombination. Thus, as the composite is irradiated by visible light, the excited electrons jumped from O 1s to the Ta5d orbital to form the $\cdot O_2^-$. The holes on the valence band can form ·OH with water molecules, which are adsorbed on the catalysts' surface. Therefore, the holes play a crucial role in the photocatalytic process, which can decompose the dye into small molecules. The addition of metals effectively inhibits the photoelectron-hole recombination

and improves the photocatalytic performance of the materials. The reaction process is as follows:

Ce-NTO +hv → e^- + h^+

e^- + O_2→$\cdot O_2^-$

h^+ + OH^-→·OH

h^+ + $\cdot O_2^-$ + ·OH + ARS→CO_2 + H_2O + Inorganic molecules.

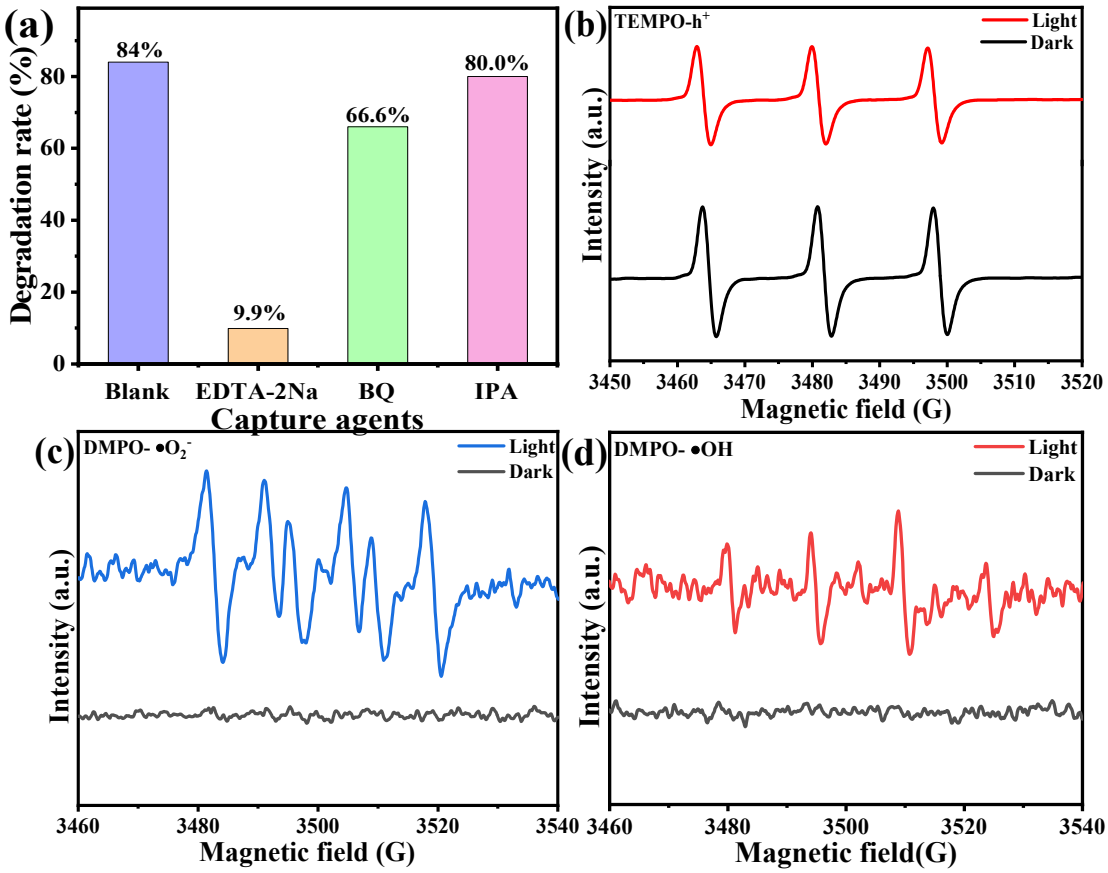

Figure 10. (**a**) Catalyst radical capture experiment; (**b**) DMPO-h^+; (**c**) DMPO-O_2^-; (**d**) DMPO-OH.

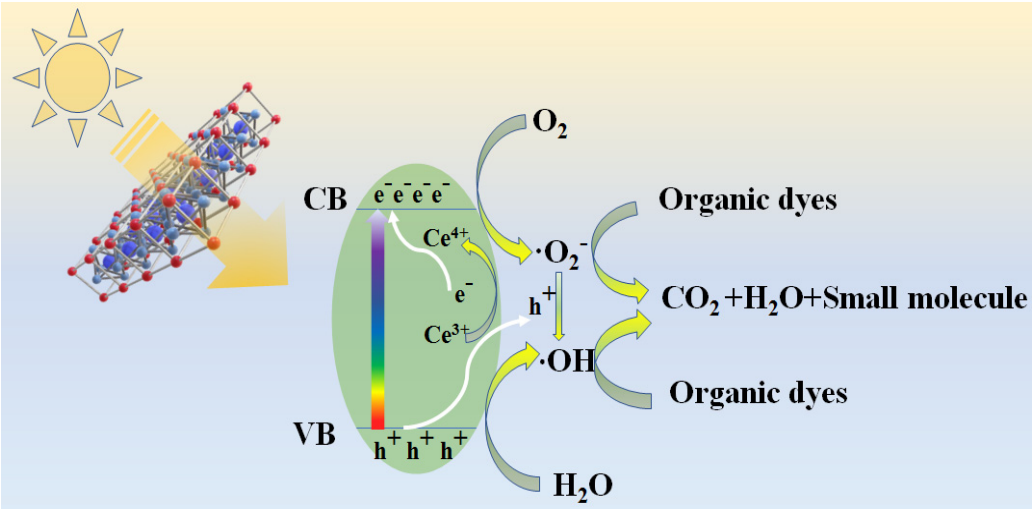

Figure 11. Schematic diagram of possible reactions of Ce-NTO degradation system.

3. Conclusions

The series $NaTaO_3$ perovskite modified with five different metal elements were prepared with the hydrothermal method and applied for photocatalytic degradation. The structural test results indicate that Na^+ was partially replaced by Bi and Ce in the A-position of the perovskite. In addition, Fe, Ni and Mn partially replace Ta^{5+} doped into the B-position of $NaTaO_3$. The metal doping forms an intermediate energy band, which reduces the band gap of NTO and decreases the photogenerated electron-hole recombination rate. The Ce-NTO sample showed the best photocatalytic degradation performance with a narrower band gap, high migration rate of photogenerated carriers and weak recombination of photogenerated charges and holes. The holes play a crucial role in the photocatalytic process, which can decompose the dye into small molecules.

4. Materials and Methods

4.1. Preparation of Photocatalysts

Referring to the traditional hydrothermal method with sodium hydroxide and tantalum pentoxide as raw materials, according to the ratio Ta:M (M = Fe, Ce, Ni, Mn, Bi) = 9:1 indicating the amount of material to add, a certain amount of nitric acid substances (iron nitrate, cerium nitrate, nickel nitrate, manganese nitrate, bismuth nitrate) was dissolved in deionized water, and the mixed solution was placed in a stainless steel reactor liner at 140 °C for 12 h. Then, the metal-doped $NaTaO_3$ product is obtained by thoroughly washing until neutral and removing impurities. The aimed materials were dried in an oven at 80 °C for 12 h and further calcined at 700 °C for 4 h in a muffle furnace.

4.2. Characterization of Photocatalysts

The crystal structure and microcrystal size of the materials were recorded by XRD patterns to investigate the effect of doping on the crystalline structure of the catalyst. The test instrument was a D8 ADVANCE A25 X-ray diffraction from Bruker AXS GmbH, Karlsruhe, Germany. The test parameters were Cu Kα-rays with an incident wavelength of λ = 0.15418 nm, a test voltage of 60 kV, a test current of 80 mA and a range of 10–85°.

The infrared spectroscopy instrument is a PerkinElmer Fourier transform infrared spectrometer, model Spectrum Two, Waltham, MA, USA.

The catalyst surface oxygen species as well as the dopant elements were examined by XPS results for species, content, and valence state. The XPS test instrument was a Thermo Scientific K-Alpha X-ray photoelectron spectrometer, Waltham, MA, USA, with an X-ray source: 12 kV, 6 mA current, 400 μm beam spot diameter, 100 eV flux energy, 16 kV operating voltage and 14.9 mA current. The charge calibration was performed with C1s = 284.8 eV.

The diffuse reflectance spectra of the samples were obtained using a UV-Vis diffuse reflectance spectrometer (Shimadzu UV-2700, Kyoto, Japan) with a test range of 200 nm–800 nm.

The surface morphology, shape, size and distribution of the sample particles were studied by SEM. The SEM test model was a ZEISS Sigma 300 SEM from Oberkochen, Germany. The acceleration voltage was 3 kV for the morphology shot, 15 kV for the energy spectrum mapping shot, and the detector was a SE2 secondary electron detector. The morphology of the material was photographed by transmission electron microscopy (TEM) with high resolution. The model used was JEOL JEM-F200, Kyoto, Japan, the accelerating voltage was 200 kV, and the energy spectrum model was JED-2300T, Kyoto, Japan.

A fluorescence emission spectrometer (PL Edinburgh FLS1000, Edinburgh, UK) was used to analyze the photoexcited electron-hole recombination rate and photoelectron conduction efficiency of the catalyst materials. The excitation wavelength used was 385 nm.

The EPR signals of the catalysts in both dark and light conditions were detected using the EPR 200M instrument of the GOKI Quantum, Hefei, China.

The transient surface photocurrent was used to characterize the surface photocurrent intensity of the material and thus analyze the photoelectron transport.

4.3. Photocatalytic Degradation

4.3.1. Photocatalytic Activity Test

A full-wavelength 300 W xenon lamp was used as the light source, and a solution with a concentration of 20 mg/L was prepared by dissolving 20 mg of dye in 1 L of water and stirring the solution vigorously to ensure complete dissolution. The 20 mg of catalyst was first dispersed in a configured 50 mL of contaminant solution, and then the contaminant solution was placed on a magnetic stirrer used to make the solution uniformly dispersed and stirred in the dark for 30 min to reach adsorption equilibrium. During the photocatalytic process, 3 mL of supernatant was aspirated every 15 min at specified time intervals, and the solution was filtered using a 0.22 μm microporous filter tip to filter the catalyst, before the solution was analyzed by UV-vis spectrophotometer. Alizarin red wavelength maximum absorption λ = 263, and methylene blue maximum absorption wavelength λ = 664.

$$\eta = \frac{C_0 - C}{C_0} \times 100\% \quad (1)$$

C_0-initial concentration of the solution (mg/L); C-concentration of the solution at the time of reaction (mg/L).

4.3.2. Catalyst Kinetics Study

In photocatalysis, degradation kinetics have been extensively studied and most kinetic models are based on the Langmuir-Hinshelwood equation, as follows:

$$\ln \frac{C_0}{C} = kt \quad (2)$$

C_0 is the initial concentration of the pollutant after adsorption equilibrium (mg/L); C is the concentration at time t of the photocatalytic reaction (mg/L); and k is the first-order reaction rate constant (min^{-1}).

Supplementary Materials: The following supporting information can be downloaded at: https://www.mdpi.com/article/10.3390/catal13091250/s1, Figure S1. O 1s profiles of (a–f) $NaTaO_3$ and M-$NaTaO_3$ (M=Fe, Ce, Ni, Mn, Bi) series catalysts; Figure S2. High-resolution XPS patterns of Fe 2p, Ce 3d, Ni 2p, Mn 2p, Bi 4f of catalysts; Figure S3. (a–f) VB XPS spectrum of the catalysts; Figure S4. Photocatalytic degradation ARS kinetics. (a) all sample within 120 min, (b) Ce-NTO and Ni-NTO within 60 min.

Author Contributions: A.H.: Investigation, Writing—Original Draft, Formal analysis, Visualization. H.Z.: Conceptualization, Formal analysis, Writing—Review and Editing, Funding acquisition. M.W.: Formal analysis, Visualization. Y.Z.: Formal analysis, Visualization. S.B.: Formal analysis, Funding acquisition. W.L.: Methodology, Conceptualization. F.L.: Methodology, Conceptualization, Writing—Review and Editing. All authors have read and agreed to the published version of the manuscript.

Funding: This research was funded by Natural Science Foundation of Ningxia Province (No. 2023AAC03015), the National Natural Science Foundation of China (No. 21862013) and the Natural Science Foundation of Ningxia Province (No. 2022AAC03046).

Data Availability Statement: The data presented in this study are available within the article and Supplementary Materials.

Acknowledgments: This work was financially supported by the Natural Science Foundation of Ningxia Province (No. 2023AAC03015), the National Natural Science Foundation of China (No. 21862013) and the Natural Science Foundation of Ningxia Province (No. 2022AAC03046).

Conflicts of Interest: The authors declare no conflict of interest.

References

1. Saravanan, A.; Kumar, P.S.; Jeevanantham, S.; Anubha, M.; Jayashree, S. Degradation of toxic agrochemicals and pharmaceutical pollutants: Effective and alternative approaches toward photocatalysis. *Environ. Pollut* **2022**, *298*, 118844. [CrossRef] [PubMed]
2. He, M.; Xu, Z.; Hou, D.; Gao, B.; Cao, X.; Ok, Y.S.; Rinklebe, J.; Bolan, N.S.; Tsang, D.C.W. Waste-derived biochar for water pollution control and sustainable development. *Nat. Rev. Earth Environ.* **2022**, *3*, 444–460. [CrossRef]
3. Ahmadijokani, F.; Molavi, H.; Bahi, A.; Fernández, R.; Alaee, P.; Wu, S.; Wuttke, S.; Ko, F.; Arjmand, M. Metal-Organic Frameworks and Electrospinning: A Happy Marriage for Wastewater Treatment. *Adv. Funct. Mater.* **2022**, *32*, 2207723. [CrossRef]
4. Yan, H.; Lai, C.; Wang, D.; Liu, S.; Li, X.; Zhou, X.; Yi, H.; Li, B.; Zhang, M.; Li, L.; et al. In situ chemical oxidation: Peroxide or persulfate coupled with membrane technology for wastewater treatment. *J. Mater. Chem. A* **2021**, *9*, 11944–11960. [CrossRef]
5. Ma, Y.; Huang, J.; Han, T.; Li, R.; Cao, M.; Li, X. A comprehensive study on the exposure of nanoplastics to constructed wetland ecological systems: Macrophyte physiology and microbial enzymology, community composition and metabolic functions. *Chem. Eng. J.* **2022**, *434*, 134592. [CrossRef]
6. Poonia, K.; Singh, P.; Singh, A.; Thakur, S.; Van Le, Q.; Ahamad, T.; Raizada, P.; Wang, C.; Nguyen, L.H.; Nguyen, V.-H. Photoelectrocatalytic systems for simultaneous energy recovery and wastewater treatment: A review. *Environ. Chem. Lett.* **2022**, *21*, 265–283. [CrossRef]
7. Feijoo, S.; Yu, X.; Kamali, M.; Appels, L.; Dewil, R. Generation of oxidative radicals by advanced oxidation processes (AOPs) in wastewater treatment: A mechanistic, environmental and economic review. *Rev. Environ. Sci. Bio/Technol.* **2023**, *22*, 205–248. [CrossRef]
8. Li, K.; Wang, H.; Li, J.; Dong, F. Design and mechanism of photocatalytic oxidation for the removal of air pollutants: A review. *Environ. Chem. Lett.* **2022**, *20*, 2687–2708. [CrossRef]
9. Saad, I.; Ralha, N.; Abukhadra, M.R.; Al Zoubi, W.; Ko, Y.G. Recent advances in photocatalytic oxidation techniques for decontamination of water. *J. Water Process Eng.* **2023**, *52*, 103572. [CrossRef]
10. Nunes, D.; Pimentel, A.; Branquinho, R.; Fortunato, E.; Martins, R. Metal Oxide-Based Photocatalytic Paper: A Green Alternative for Environmental Remediation. *Catalysts* **2021**, *11*, 504. [CrossRef]
11. Lee, S.L.; Chang, C.-J. Recent Progress on Metal Sulfide Composite Nanomaterials for Photocatalytic Hydrogen Production. *Catalysts* **2019**, *9*, 457. [CrossRef]
12. Chen, W.-Y.; Wang, C.-P.; Chen, P.-C.; Lin, K.-Y.A.; Ghosh, S.; Huang, C.-W.; Nguyen, V.-H. Perovskite Zinc Titanate Photocatalysts Synthesized by the Sol–Gel Method and Their Application in the Photocatalytic Degradation of Emerging Contaminants. *Catalysts* **2021**, *11*, 854. [CrossRef]
13. Ke, P.; Zeng, D.; Cui, J.; Li, X.; Chen, Y. Improvement in Structure and Visible Light Catalytic Performance of g-C_3N_4 Fabricated at a Higher Temperature. *Catalysts* **2022**, *12*, 247. [CrossRef]
14. Hou, J.; Cao, S.; Wu, Y.; Liang, F.; Ye, L.; Lin, Z.; Sun, L. Perovskite-based nanocubes with simultaneously improved visible-light absorption and charge separation enabling efficient photocatalytic CO_2 reduction. *Nano Energy* **2016**, *30*, 59–68. [CrossRef]
15. Xu, Y.; Li, H.; Sun, B.; Qiao, P.; Ren, L.; Tian, G.; Jiang, B.; Pan, K.; Zhou, W. Surface oxygen vacancy defect-promoted electron-hole separation for porous defective ZnO hexagonal plates and enhanced solar-driven photocatalytic performance. *Chem. Eng. J.* **2020**, *379*, 122295. [CrossRef]
16. Zhou, H.; Yin, Q. Hydrothermal preparation of Nb-doped $NaTaO_3$ with enhanced photocatalytic activity for removal of organic dye. *Chin. J. Chem. Eng.* **2022**, *46*, 142–149. [CrossRef]
17. Li, X.; Zang, J. Hydrothermal synthesis and characterization of Lanthanum-doped $NaTaO_3$ with high photocatalytic activity. *Catal. Commun.* **2011**, *12*, 1380–1383. [CrossRef]
18. Wang, C.; Zhang, Y.; Liu, Y.; Chen, Q.; Song, Y.; Cai, A.; Guo, H.; Zhang, P. Photocatalytic and antibacterial properties of $NaTaO_3$ nanofilms doping with Mg^{2+}, Ca^{2+} and Sr^{2+}. *Appl. Surf. Sci.* **2023**, *612*, 155881. [CrossRef]
19. Zhu, J.; Li, H.; Zhong, L.; Xiao, P.; Xu, X.; Yang, X.; Zhao, Z.; Li, J. Perovskite Oxides: Preparation, Characterizations, and Applications in Heterogeneous Catalysis. *ACS Catal.* **2014**, *4*, 2917–2940. [CrossRef]
20. Grabowska, E. Selected perovskite oxides: Characterization, preparation and photocatalytic properties—A review. *Appl. Catal. B Environ.* **2016**, *186*, 97–126. [CrossRef]
21. Wang, X.; Bai, H.; Meng, Y.; Zhao, Y.; Tang, C.; Gao, Y. Synthesis and optical properties of Bi^{3+} doped $NaTaO_3$ nano-size photocatalysts. *J. Nanosci. Nanotechnol.* **2010**, *10*, 1788–1793. [CrossRef] [PubMed]
22. Loryuenyong, V.; Totepvimarn, K.; Eimburanapravat, P.; Boonchompoo, W.; Buasri, A. Preparation and Characterization of Reduced Graphene Oxide Sheets via Water-Based Exfoliation and Reduction Methods. *Adv. Mater. Sci. Eng.* **2013**, *2013*, 923403. [CrossRef]
23. Shanker, V.; Samal, S.L.; Pradhan, G.K.; Narayana, C.; Ganguli, A.K. Nanocrystalline $NaNbO_3$ and $NaTaO_3$: Rietveld studies, Raman spectroscopy and dielectric properties. *Solid State Sci.* **2009**, *11*, 562–569. [CrossRef]
24. Cui, H.; Shi, J.; Liu, H. Influence of Bi chemical state on the photocatalytic performance of Bi-doped $NaTaO_3$. *Chin. J. Catal.* **2015**, *36*, 969–974. [CrossRef]
25. Tüysüz, H.; Chan, C.K. Preparation of amorphous and nanocrystalline sodium tantalum oxide photocatalysts with porous matrix structure for overall water splitting. *Nano Energy* **2013**, *2*, 116–123. [CrossRef]
26. Sudrajat, H.; Babel, S.; Thushari, I.; Laohhasurayotin, K. Stability of La dopants in $NaTaO_3$ photocatalysts. *J. Alloys Compd.* **2019**, *775*, 1277–1285. [CrossRef]

27. Dong, C.L.; Sun, H.; Zhou, Y.; Zhan, H.J.; Wang, G.; Liu, W.Y.; Bi, S.X.; Ma, B.J. Transition metal (Ni, Cu, Ga, Fe) doped $LaCoO_3$ improve surface hydrogen activation to promote low-temperature CO_2 methanation, J. *Environ. Chem. Eng.* **2022**, *10*, 107718. [CrossRef]
28. Al-Bassami, N.S.; Mansour, S.F.; Abdel-Fattah, E.; Abdo, M.A. Ce-Co-Mn-Zn ferrite nano catalyst: A synergetic effect of rare earth Ce^{3+} on enhanced optical properties and photocatalysis. *Ceram. Int.* **2023**, *49*, 20601–20612. [CrossRef]
29. Pozan, G.S.; Kambur, A. Removal of 4-chlorophenol from wastewater: Preparation, characterization and photocatalytic activity of alkaline earth oxide doped TiO_2. *Appl. Catal. B Environ.* **2013**, *129*, 409–415. [CrossRef]
30. Jana, P.; Mata Montero, C.; Pizarro, P.; Coronado, J.M.; Serrano, D.P.; de la Peña O'Shea, V.A. Photocatalytic hydrogen production in the water/methanol system using Pt/RE:$NaTaO_3$ (RE = Y, La, Ce, Yb) catalysts. *Int. J. Hydrog. Energy* **2014**, *39*, 5283–5290. [CrossRef]